Effect of ideal internal MHD instabilities on NBI fast ion redistribution in ITER 15 MA scenario

Guanming YANG (杨冠铭)[1] , **Yueqiang LIU** (刘钺强)[2], **Zhibin WANG** (王志斌)[3],
Yongqin WANG (王雍钦)[1], **Yutian MIAO** (苗雨田)[1] and
Guangzhou HAO (郝广周)[1,*]

[1] Southwestern Institute of Physics, Chengdu 610041, People's Republic of China
[2] General Atomics, San Diego, CA 92186-5608, United States of America
[3] Sino-French Institute of Nuclear Engineering and Technology, Sun Yat-sen University, Zhuhai 519082, People's Republic of China

E-mail: haogz@swip.ac.cn

CrossMark

Abstract

Transport of fast ions is a crucial issue during the operation of ITER. Redistribution of neutral beam injection (NBI) fast ions by the ideal internal magnetohydrodynamic (MHD) instabilities in ITER is studied utilizing the guiding-center code ORBIT (White R B and Chance M S 1984 *Phys. Fluids* **27** 2455). Effects of the perturbation amplitude A of the internal kink, the perturbation frequency f of the fishbone instability, and the toroidal mode number n of the internal kink are investigated, respectively, in this work. The $n = 1$ internal kink mode can cause NBI fast ions transporting in real space from regions of $0 < s \leqslant 0.32$ to $0.32 < s \leqslant 0.53$, where s labels the normalized plasma radial coordinate. The transport of fast ions is greater as the perturbation amplitude increases. The maximum relative change of the number of fast ions approaches 5% when the perturbation amplitude rises to 500 G. A strong transport is generated between the regions of $0 < s \leqslant 0.05$ and $0.05 < s \leqslant 0.12$ in the presence of the fishbone instability. Higher frequency results in greater transport, and the number of fast ions in $0 < s \leqslant 0.05$ is reduced by 30% at the fishbone frequency of 100 kHz. Perturbations with higher n will lead to the excursion of fast ion transport regions outward along the radial direction. The loss of fast ions, however, is not affected by the internal MHD perturbation. Strong transport from $0 < s \leqslant 0.05$ to $0.05 < s \leqslant 0.12$ does not influence the plasma heating power of ITER, since the NBI fast ions are still located in the plasma core. On the other hand, the influence of fast ion transport from $0 < s \leqslant 0.32$ to $0.32 < s \leqslant 0.53$ needs further study.

Keywords: ITER, NBI fast ions, internal kink mode, fishbone instability, ORBIT

(Some figures may appear in colour only in the online journal)

1. Introduction

Generated either from fusion reactions, or from auxiliary heating like neutral beam injection (NBI), ion cyclotron radio frequency wave, and low hybrid wave, the fast ions are usually highly populated in the center of the plasma and play an important role in the plasma heating [1, 2]. The magneto-hydrodynamic (MHD) instabilities in tokamaks, however, will interact with fast ions and result in the transport and loss of fast ions from the core region to the edge of the plasma. This degraded confinement of fast ions has a significant impact on the fusion power and plasma properties. It will not only reduce the fusion power and energy gain of tokamaks, but also cause the degradation of plasma confinement performance and damage to the first wall.

---

* Author to whom any correspondence should be addressed.

Therefore, the transport of fast ions is a critical issue for present tokamaks and future fusion devices such as ITER [3, 4].

Due to the importance of this topic, the transport of fast ions has been studied for many years [5]. With the development of tokamak devices and theoretical models, both experiment and simulation works have been extensively carried out to study the conditions and mechanism of fast ion transport. In several tokamak devices, the transport and loss of fast ions induced by various MHD instabilities have been investigated [6–10]. Besides the experimental investigations, the modeling works are devoted to analyzing the experimental data and relevant physical processes, which contribute to continuous progress in the understanding of fast ion transport in recent years. Based on the experimental results of DIII-D, several simulation works are carried out utilizing the codes ORBIT, M3D-C1, OFSEF and TRANSP to study the NBI fast ion transport [11–13]. The fast ion redistribution triggered by sawtooth instability is also investigated with the codes M3D-K and ORBIT [14, 15]. The effects of other MHD instabilities, like toroidal field (TF) ripples, neoclassical tearing mode [16] and ion temperature gradient driven mode [17], on fast ion transport are studied with original theoretical models. Moreover, the numerical simulation is a crucial solution for fast ion transport study during the design of future tokamak devices in the absence of experimental conditions. For instance, the codes ASCOT, SPIRAL and ORBIT are utilized to study the TF ripple-induced fusion alpha transport in SPARC [18] and CFETR [19].

Among the existing and future tokamak devices, ITER is the most promising device to demonstrate controlled fusion energy. In the design of ITER, the fast ions generated from NBI are the main external heating method to maintain plasma heating power and achieve high energy gain [2]. Different from the energy of about 100 keV in other tokamak devices, the energy of NBI fast ions in ITER is about 1 MeV due to the heating requirement [20]. With this high energy, NBI fast ions are able to penetrate into the central region and heat the bulk plasma there. On the other hand, the plasma current in ITER is designed to be 15 MA in the D-T fusion scenario [21]. This high current may lead to a burst of the internal kink mode in the plasma core. Meanwhile, the fishbone instability can be excited by the interaction of fast ions with the internal kink mode [22]. The relevant simulation works have been extensively carried out, for instance, the investigations of NBI transport and loss in ITER by radial electric field [23] and RMPs [24, 25]. Redistribution of alpha particles by internal kink and sawtooth is studied with circular cross section and ITER-like parameters [26–28]. Fast ion transport by fishbone is simulated for a JET plasma based on the experimental measurements [22]. Besides the fast ion transport, the effects of fast ions on internal kink/fishbone have been extensively studied since the last century [29–42], which are therefore not discussed in this work.

As the NBI fast ion redistribution can be triggered by internal kink mode [28] and fishbone instability [43], the effect of internal MHD instabilities on transport and loss of NBI fast ions is also a key issue in ITER. Numerical studies on redistribution of high energy NBI fast ions by internal kink/fishbone in ITER, however, are scarce, which motivates the present study. In this work, the tracing particle orbit code ORBIT [44] is utilized to calculate the redistribution of NBI fast ions with ideal internal MHD instabilities in ITER. The initial fast ion distribution function is calculated by a time-dependent 2D Fokker–Planck solver in velocity space [45] with the first orbit averaged ion sources. The initial distribution of half a million fast ions is in accordance with the operation condition of ITER. Based on the operation parameters and high energy NBI condition in ITER, the effects of the internal kink mode and the fishbone with higher frequency, which is supposed to be a special phenomenon in ITER, are studied numerically. Three parameters are investigated, respectively: the perturbation amplitude A of the internal kink, the perturbation frequency f of the fishbone, and the toroidal mode number n of the internal kink. In this simulation, the perturbation amplitude is assumed to be $A = 100, 300, 500$ G, the perturbation frequency is assumed to be $f = 0, 20, 40, 60, 80, 100$ kHz, and the toroidal mode numbers are $n = 1, 2, 3, 4$. Closely related to internal kink mode, the mode structure of the fishbone is the same as that of the $m = n = 1$ internal kink [46], where m is the poloidal mode number. In the practical simulation, the internal kink mode structure is usually used to replace fishbone instability [6, 22, 43]. Hence the effect of the fishbone is simulated by adding different perturbation frequencies to the structure of the $n = 1$ internal kink. The simulation results show that the NBI fast ion redistribution is sensitive to the perturbation amplitude and frequency. The loss of NBI fast ions, however, is not affected by the perturbation amplitude, the perturbation frequency, or the toroidal mode number. The structure of this paper is as follows. Section 2 briefly introduces the code ORBIT. Section 3 presents the initial distribution data of NBI fast ions and the structures of internal kink perturbation applied with different n. In section 4, the simulation of NBI fast ion redistribution by ideal internal MHD instabilities is performed. Section 5 summarizes the results.

2. Modeling approach of ORBIT code

The effects of internal kink mode on the redistribution of NBI fast ions in ITER are simulated using the tracing particle orbit code ORBIT [44]. The code traces and calculates the position and velocity of particles in plasma by solving guiding center orbit equations. From the Hamiltonian quantities, Lagrangian quantities, Lagrangian equations and magnetic field expressions for guiding center drift motion without perturbation, the equations of particle motion without perturbation can be derived. If the magnetic field perturbation is considered, the canonical momentum, Hamiltonian, poloidal and toroidal canonical momentum will be modified and new motion equations can be obtained [44, 47]. The specific expressions and equations are presented in the appendix. By solving the particle guiding center motion equations with the fourth-order Runge–Kutta method, ORBIT can trace the position and velocity of particles and then obtain their orbits and distribution.
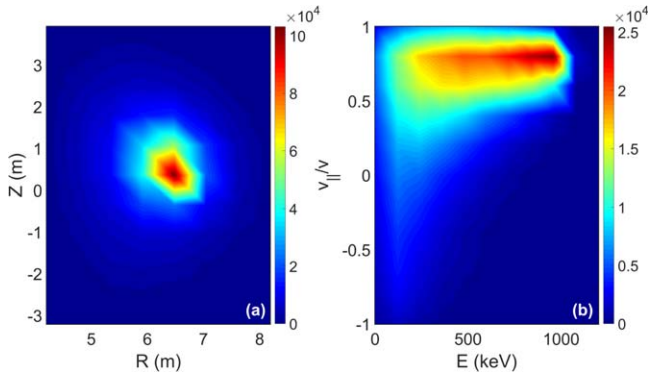
Figure 1. Distribution of half a million of NBI fast ions in ITER at the initial moment the color bar indicates the number of particles. (a) Distribution in real space, where the *R–Z* plane represents the poloidal cross section of the plasma in ITER. (b) Distribution in phase space, where *E* is the energy of fast ions, $v_{\parallel}/v$ is the pitch angle of fast ions.

3. Initial distribution of NBI fast ions and IK perturbation structures

### 3.1. Initial distribution of NBI fast ions loaded by ORBIT

The particle orbit tracing code ORBIT is utilized to simulate the effects of internal kink mode on the redistribution of NBI fast ions in ITER. In the calculation of ORBIT, this work uses the initial distribution data of half a million of NBI fast ions, which is calculated by time-dependent 2D Fokker–Planck solver in velocity space [45] with first orbit averaged ion sources, as the input data of particle distribution at the initial moment.

Figure 1 shows the distribution of half a million NBI fast ions in ITER at the initial moment. Figures 1(a) and (b) show, respectively, the initial distribution in real space and in phase space. The color bar indicates the number of particles. Figure 1(a) shows that most NBI fast ions are populated in the core region in ITER at the initial moment. Figure 1(b) shows that most NBI fast ions have a pitch angle larger than 0.5, and the number of NBI fast ions with an energy around 1 MeV is the largest. The information provided by the real and phase spaces indicates that the initial distribution is a distribution of NBI fast ions which have just been injected into ITER and have not been slowed down for a long time. Thus, the energy and pitch angle of most fast ions are centered around 1 MeV and 0.8, respectively.

3.2. IK perturbation structures assumed for ORBIT

To study the effects of internal kink mode/fishbone instability on redistribution of NBI fast ions in ITER, three instability parameters are investigated: the perturbation amplitude *A*, the perturbation frequency *f* and the toroidal mode number *n*. In the investigation of *n*, the structure of perturbation assumed for ORBIT will be changed due to the change of *n* in internal kink mode.

Figures 2(a)–(c) show the profiles of bulk plasma temperature, bulk plasma density and safety factor *q* in the ITER 15 MA scenario assumed for ORBIT. The horizontal coordinate $s \equiv \sqrt{\psi_p/\psi_w}$ represents the normalized plasma radial
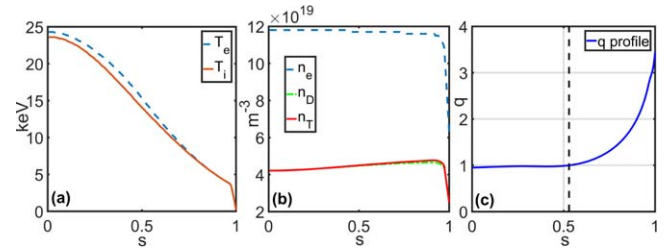
Figure 2. Profiles of (a) bulk plasma temperature, (b) bulk plasma density, (c) safety factor *q* in ITER 15 MA scenario assumed for ORBIT.

position, where ψ_p is the poloidal flux and ψ_w denotes the poloidal flux at the wall location. Thus $s = 0$ at the magnetic axis and $s = 1$ at the edge of the plasma. In plot (a), the vertical coordinate denotes the temperature of the bulk plasma in units of keV. The blue dotted and red solid curves represent, respectively, the temperature profiles of bulk electrons and bulk ions. The vertical coordinate in plot (b) indicates the density of bulk plasma in units of m^{-3}. The blue-dotted, green-dotted and red solid curves in plot (b) represent, respectively, the density profiles of bulk electrons, bulk deuterium ions and bulk tritium ions. In plot (c), the vertical coordinate is the safety factor *q*. The black vertical dotted line represents the radial position of $s = 0.53$ where the safety factor $q = 1$. In general, the safety factor *q* increases as *s* increases, while a slight negative shear presents itself in the region of $0.2 < s < 0.4$. At the position of $s = 0$, $q = 0.95$. It can be seen that $q < 1$ in the region of $s < 0.53$ and $q > 1$ in the region of $s > 0.53$.

Figure 3 presents the structure of the internal kink mode assumed for ORBIT with $n = 1, 2, 3, 4$. Figures 3(a)–(d) show the structure of perturbation displacement output by MARS-F [48]. The horizontal coordinate $s \equiv \sqrt{\psi_p/\psi_w}$ is the normalized plasma radial position. The vertical coordinate ξ(norm.amp) represents the amplitude of perturbation displacement normalized by the major poloidal mode number *m* component. The perturbation components with different *m* are represented by different color curves. The negative value represents the radial direction of perturbation displacement. It can be seen that as *n* increases, the *m* component that plays a major role in perturbation displacement structure also increases, and there is always major $m = n$. After importing the internal kink mode structure of figures 3(a)–(d) into ORBIT, the structure of radial magnetic perturbation field amplitude calculated by ORBIT is shown in figures 3(e)–(h). The vertical coordinate dB_r/B indicates the radial magnetic perturbation field amplitude normalized by the background magnetic field in ITER, which is 5.3 T. The actual perturbation amplitude used is determined by the amplitude peak of the maximum magnetic field component in figures 3(e)–(h), which can be modified in ORBIT. These two figures show that the structures of internal kink modes with different *n* are all located in the region of $s < 0.53$, which indicates the region of $q < 1$. Moreover, the peaks of internal kink perturbations shift outward along the radial direction as *n* increases.
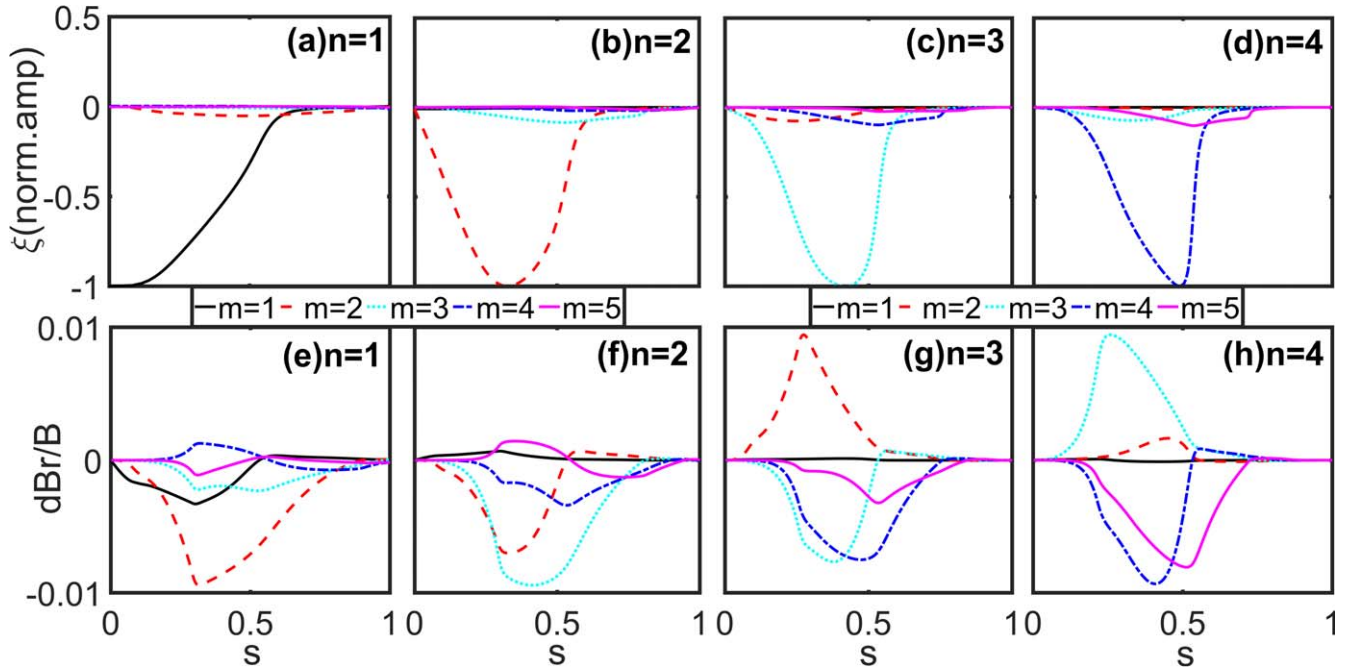
Figure 3. Structures of internal kink mode assumed for ORBIT. The first row (a)–(d) shows the structures of internal kink perturbation displacement with the toroidal mode number (a) $n = 1$, (b) $n = 2$, (c) $n = 3$, (d) $n = 4$. The second row (e)–(h) shows the structures of internal kink perturbation field amplitude with the toroidal mode number (e) $n = 1$, (f) $n = 2$, (g) $n = 3$, (h) $n = 4$.

4. NBI fast ion redistribution by IK/fishbone

4.1. Effects of perturbation amplitude on NBI fast ion redistribution

This section focuses on the effects of perturbation amplitude A on the redistribution of NBI fast ions. As the perturbation structure shown in figures 3(a) and (e), the perturbation amplitude considered here is the peak value of the radial perturbation field amplitude. The maximum perturbation amplitude is supposed as 1% of the background magnetic field, which is 5.3 T in ITER. Three different perturbation amplitudes of internal kink mode are investigated: $A = 100, 300, 500$ G. The toroidal mode number and the perturbation frequency are fixed as $n = 1$ and $f = 0$. ORBIT is utilized to calculate the redistribution of NBI fast ions after 5 ms in ITER with four cases of no perturbation and three different perturbation amplitudes.

The calculation results of ORBIT are shown in figure 4. Figures 4(a)–(c) compare, respectively, the number profiles of NBI fast ions in real space for $A = 100, 300, 500$ G perturbations with no perturbation. The vertical coordinate N indicates the number of NBI fast ions at the corresponding radial position. The blue curves represent the case without perturbation and the red curves represent the $A = 100, 300, 500$ G perturbation cases. The two black vertical dotted lines in plot (c) represent the radial positions of $s = 0.32$ and $s = 0.53$. As figure 4 shows, the NBI fast ion profiles are basically unchanged with 100 G perturbation amplitude. When the perturbation amplitude increases, the NBI fast ion profile starts to change. Considering the cases of 500 G perturbation, in the region of $0 < s \leqslant 0.32$, the effect of internal kink mode decreases the number of NBI fast ions;

in the region of $0.32 < s \leqslant 0.53$, the number of NBI fast ions increases; in the region of $s > 0.53$, the number of fast ions is almost unchanged. This indicates that some NBI fast ions move from the region of $0 < s \leqslant 0.32$ to the region of $0.32 < s \leqslant 0.53$ under the effect of perturbation. The internal kink mode causes some NBI fast ions in the core region to transport outward.

Figures 4(d)–(f) show more clearly the relationship between the degree of NBI fast ion transport and the perturbation amplitude. The vertical coordinate indicates the relative change of NBI fast ion number at the corresponding radial position in the presence of perturbation, which is calculated as:

$$\text{Relative change} = \frac{N_{\text{pert}}(s) - N_0(s)}{N_0(s)}, \qquad (1)$$

where $N_{\text{pert}}(s)$ and $N_0(s)$ label, respectively, the NBI fast ion number at the corresponding radial position s for cases with and without perturbation. It is shown that the transport of NBI fast ions from the core region to the outer part becomes more and more obvious as the perturbation amplitude increases. When the perturbation amplitude is 500 G, the maximum relative change of NBI fast ion number is close to 5%.

Figure 5 illustrates the relationship curve between the NBI fast ion loss rate and the perturbation amplitude. The loss rate is obtained by dividing the number of fast ions lost by the total number of fast ions, which is half a million. In this work, the free boundary condition is adopted for the internal kink computation. As for the fast ion tracing simulation by ORBIT, the last closed flux surface (LCFS) is assumed as the boundary, i.e. the fast ions that intersect the LCFS are considered lost. It can be seen that the perturbation amplitude
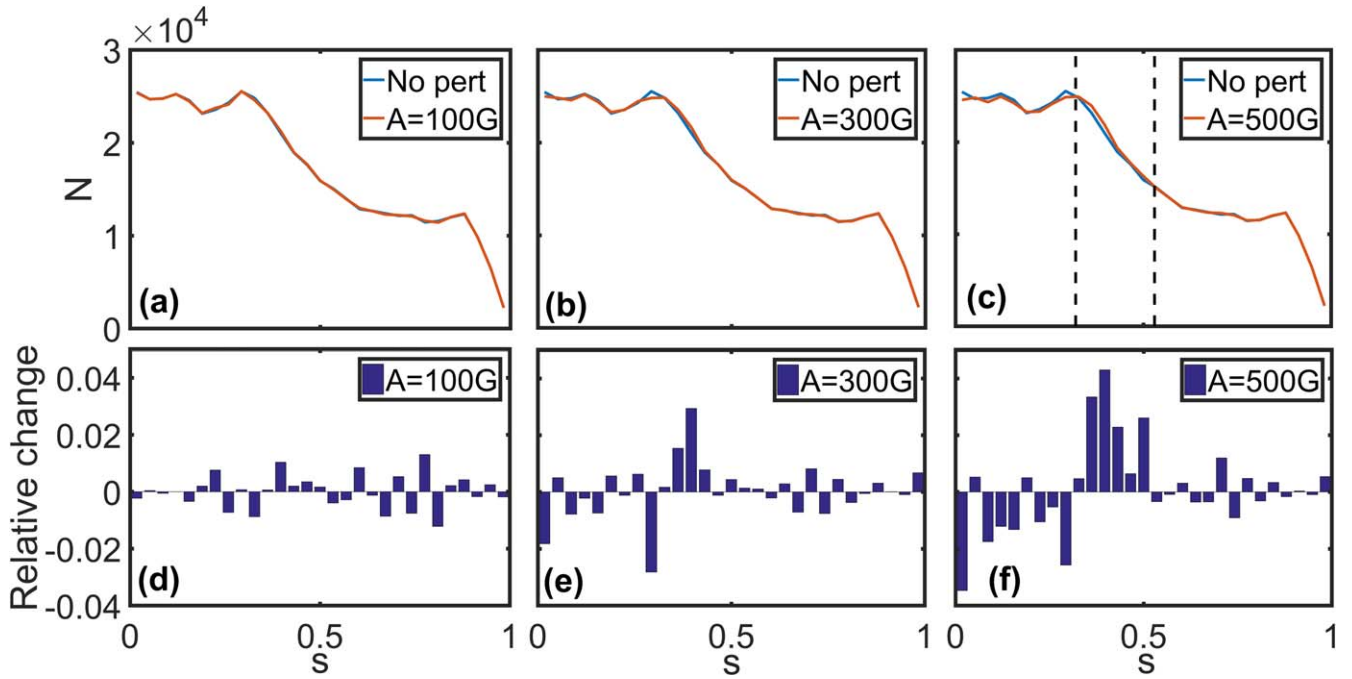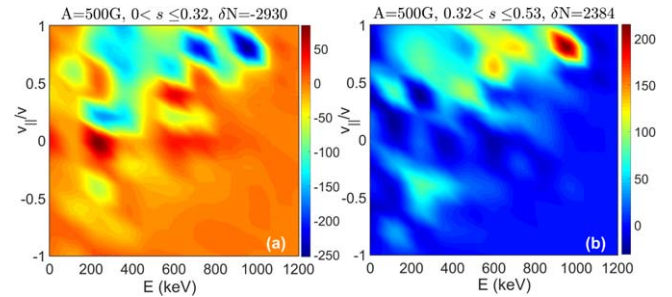
Figure 4. NBI fast ion number profiles in real space. The first row (a)–(c) presents the variation of NBI fast ion number profiles in real space in the presence of the perturbation amplitude $A=$ (a) 100 G, (b) 300 G, (c) 500 G internal kink perturbations (the perturbation frequency $f = 0$, the toroidal mode number $n = 1$). The second row (d)–(f) presents the relative change of NBI fast ion number in real space in the presence of the perturbation amplitude $A=$ (d) 100 G, (e) 300 G, (f) 500 G internal kink perturbations.
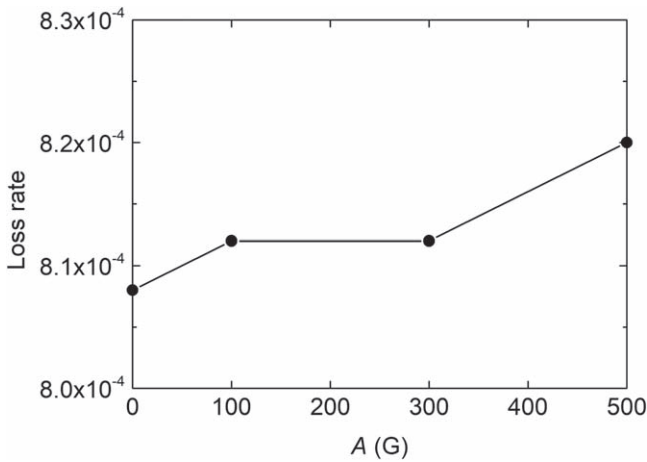
Figure 5. Relationship of NBI fast ion loss rate and perturbation amplitude A. The fast ions are considered as lost once they intersect the last closed flux surface (LCFS).

Figure 6. Distribution of NBI fast ion number change in the particle phase space ($E − v_\parallel/v$ plane) in the presence of the perturbation amplitude $A = 500$ G, the perturbation frequency $f = 0$, the toroidal mode number $n = 1$ internal kink perturbation. (a) Distribution in the real region of the radial position $0 < s \leqslant 0.32$. (b) Distribution in the real region of the radial position $0.32 < s \leqslant 0.53$.

basically does not affect the number of fast ions lost. This is because the internal kink mode perturbation occurs in the core region in ITER, and the NBI fast ions are mainly transported from $0 < s \leqslant 0.32$ to $0.32 < s \leqslant 0.53$ in the presence of perturbation. Therefore, increasing the perturbation amplitude has essentially no effect on the loss of NBI fast ions.

The redistribution of NBI fast ions in the particle phase space with 500 G perturbation is shown in figure 6. Figure 6(a) corresponds to the real space region of $0 < s \leqslant 0.32$ and figure 6(b) corresponds to the region of $0.32 < s \leqslant 0.53$. The horizontal coordinate in the figures is the fast ion energy in keV, the vertical coordinate is the pitch

angle of fast ions. The color bar represents the number of increases or decreases of NBI fast ions in the presence of 500 G perturbation compared with the no perturbation case. The δN represents the total increase or total decrease of NBI fast ions in the corresponding real space region.

Figure 6(a) shows that in the region of $0 < s \leqslant 0.32$, NBI fast ions with energy close to 1 MeV and a pitch angle of about 0.8 decreases the most, followed by NBI fast ions with energy of about 600 to 800 keV. Figure 6(b) shows that in the region of $0.32 < s \leqslant 0.53$ the number of NBI fast ions with an energy around 1 MeV and pitch angle around 0.8 decreases the most, followed by a slight increase in NBI fast ions with energy between 600 and 800 keV. Combining the phase space information in figure 6, it can be learned that most NBI fast

ions transported from $0 < s \leqslant 0.32$ to $0.32 < s \leqslant 0.53$ in the presence of 500 G perturbation have an energy around 1 MeV and a pitch angle of around 0.8. This is exactly the class of NBI fast ions with the largest number in the initial distribution data. At the same time, the fast ion energy and pitch angle do not change after transport, indicating that the type of fast ion orbit remains the same. But the orbit radius of the fast ion increases, making the fast ion transport outward.

In the region with the largest change of NBI fast ion number in figure 6, the fast ion with an energy of 960 keV and pitch angle of 0.8 is selected. The real-space Poincaré diagrams of NBI fast ion are presented in figure 7. Figures 7(a) and (b) show, respectively, the cases without perturbation and with 500 G perturbation. The vertical coordinate θ in figure 7(a) represents the poloidal angle of the fast ion. Each vertical line represents the fast ion orbit on different magnetic surfaces. There is no transport phenomenon without perturbation. The poloidal angle of the fast ion is constantly changing while the radial position remains unchanged during
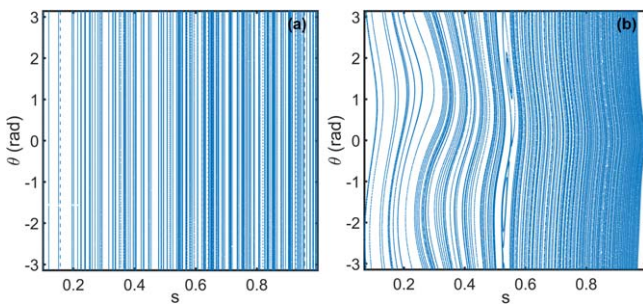

Figure 7. Real-space Poincaré diagram of NBI fast ion drift orbits with $E = 960$ keV and $v_\parallel/v = 0.8$. (a) Case without perturbation. (b) Case with the perturbation amplitude $A = 500$ G, the perturbation frequency $f = 0$, the toroidal mode number $n = 1$ internal kink perturbation.

its motion, so the fast ion orbit is represented as vertical lines in the Poincaré diagram. In figure 7(b), the fast ion orbits are distorted in the presence of 500 G internal kink mode perturbation, while the magnetic island structure capable of enhancing transport appears. The distortion of orbits represents a change in the radial position of the fast ion during its movement. The appearance of two magnetic islands represents the predominant role of the $m = 2$ component in all the magnetic perturbation field components, which is consistent with the structure of magnetic perturbation assumed for ORBIT in figure 3(e).
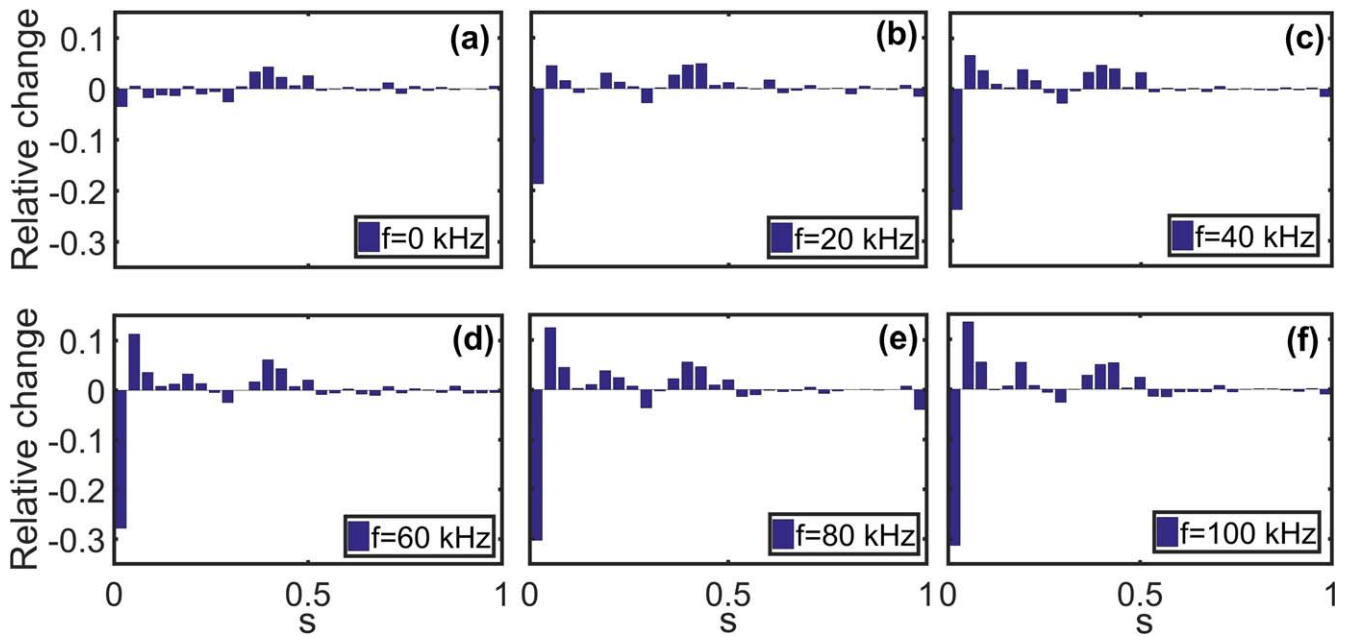
4.2. Effects of perturbation frequency on NBI fast ion redistribution

In this section, the effect of different mode perturbation frequencies f on the redistribution of NBI fast ions will be investigated. In the previous experiments on existing tokamak devices, the fishbone frequencies measured are in the range of 10–20 kHz [43, 49–52]. With a high-power NBI (injection power of 0.95 MW and fast ion energy of 40 keV), the fishbone frequencies measured on HL-2A can reach up to 30 kHz [53]. In the burning plasmas, the maximum fishbone frequency evaluated for TFTR is about 100 kHz [54]. As the NBI power (33 MW) and fast ion energy (1 MeV) in ITER [20] are much higher than those of existing tokamaks, the fishbone frequency in ITER is supposed to be higher than 20 kHz. Hence the perturbation frequencies $f = 0, 20, 40, 60, 80, 100$ kHz are selected to calculate the distribution of NBI fast ions after 5 ms of evolution, with the toroidal mode number $n = 1$ and the perturbation amplitude $A = 500$ G fixed. Since changing the frequency does not affect the mode perturbation structure, ORBIT in this section uses the same perturbation structure of figures 3(a) and (e).

The calculation results of ORBIT are shown in figures 8 and 9. Figure 8 compares the number profiles of NBI fast ions
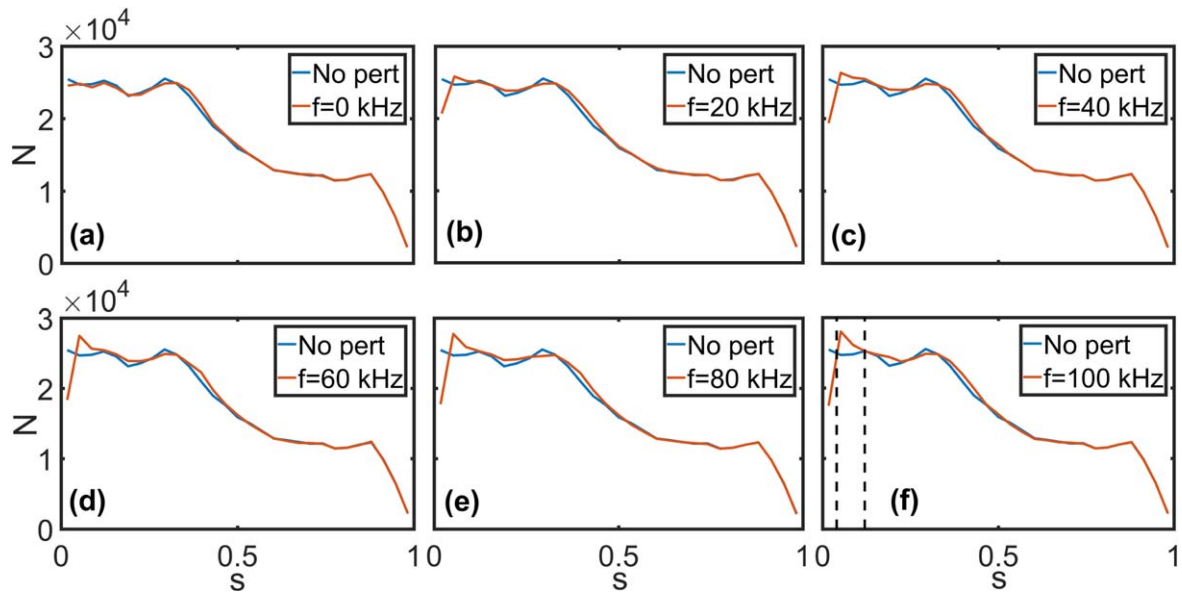
Figure 8. Variation of NBI fast ion number profiles in real space in the presence of perturbations with the perturbation frequency $f =$ (a) 0 kHz (the perturbation amplitude $A = 500$ G, the toroidal mode number $n = 1$ internal kink perturbation), (b) 20 kHz, (c) 40 kHz, (d) 60 kHz, (e) 80 kHz, (f) 100 kHz ($A = 500$ G, $n = 1$ fishbone perturbation).

Figure 9. Relative change of NBI fast ion number in real space in the presence of perturbations with the perturbation frequency $f=$ (a) 0 kHz (the perturbation amplitude $A = 500$ G, the toroidal mode number $n = 1$ internal kink perturbation), (b) 20 kHz, (c) 40 kHz, (d) 60 kHz, (e) 80 kHz, (f) 100 kHz ($A = 500$ G, $n = 1$ fishbone perturbation).

in real space with six different perturbation frequencies and without perturbation. The two black vertical dotted lines in plot (f) represent the radial positions of $s = 0.05$ and $s = 0.12$. The NBI fast ions under 0 kHz perturbation are mainly transported from $0 < s \leqslant 0.32$ to $0.32 < s \leqslant 0.53$. As the perturbation frequency increases, the transport in the outer region is essentially unchanged, but the transport in the inner region is more variable. The number of NBI fast ions in the region of $0 < s \leqslant 0.05$ decreases substantially under the effect of perturbation with frequencies, while in the regions of $0.05 < s \leqslant 0.12$ and $0.15 < s \leqslant 0.25$ the number of fast ions increases. This means that the NBI fast ions will transport from $0 < s \leqslant 0.05$ to $0.05 < s \leqslant 0.12$ and $0.15 < s \leqslant 0.25$ under the effect of perturbation with frequencies compared to the case without frequency.

Figure 9 shows the relative change of NBI fast ion number in real space with different perturbation frequencies. The transport phenomenon of NBI fast ions from $0 < s \leqslant 0.05$ to $0.05 < s \leqslant 0.12$ can be clearly seen, and the extent of fast ion transport in this region increases as the perturbation frequency increases. The relative decrease of NBI fast ion number in the region of $0 < s \leqslant 0.05$ can reach 30% with the influence of 100 kHz perturbation.

Although the transport of NBI fast ions in the inner region in the presence of high-frequency perturbations is severe, the radial position of this massive transport of fast ions is small and still located in the plasma core region. Therefore, in the absence of transport out of the plasma core, this large transport of NBI fast ions does not affect the NBI heating power and fusion condition in ITER.

Figure 10 presents the relationship curve between the NBI fast ion loss rate and the perturbation frequency. It can be seen in the figure that the variation of NBI fast ion loss rate
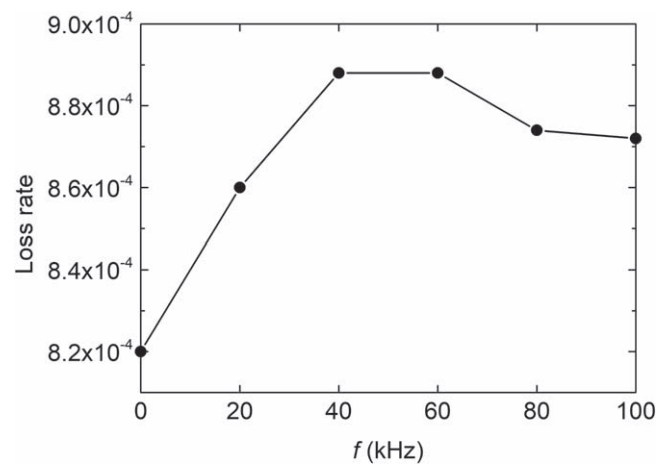

Figure 10. Relationship of NBI fast ion loss rate and perturbation frequency *f*. The fast ions are considered as lost once they intersect the LCFS.

with the change of perturbation frequency is extremely small. In the background of half a million NBI fast ions, the maximum variation of the number of fast ions lost between different perturbation frequencies does not exceed 50. Thus the loss of NBI fast ions is considered to be unaffected by the perturbation frequency.

As different fishbone frequencies are investigated here, the resonance between the mode and the fast ions indeed affects the fast ion transport. This resonant interaction depends on the mode frequency and the assumed initial distribution of fast ions. In this work, such resonance is partially taken into account. In this subsection, the 3D perturbation structure (internal kink mode with $n = 1$) and amplitude ($A = 500$ G) are fixed, while scanning the mode frequency
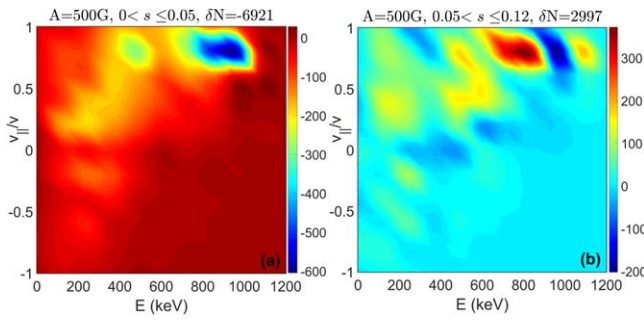
Figure 11. Distribution of NBI fast ion number change in the particle phase space ($E - v_{\parallel}/v$ plane) in the presence of the perturbation amplitude $A = 500$ G, the perturbation frequency $f = 100$ kHz, the toroidal mode number $n = 1$ fishbone perturbation. (a) Distribution in the real region of the radial position $0 < s \leqslant 0.05$. (b) Distribution in the real region of the radial position $0.05 < s \leqslant 0.12$.

Figure 12. Orbits of single NBI fast ion on the R–Z plane in the presence of perturbations with the perturbation frequency (a) $f = 0$ kHz (the perturbation amplitude $A = 500$ G, the toroidal mode number $n = 1$ internal kink perturbation), (b) $f = 100$ kHz ($A = 500$ G, $n = 1$ fishbone perturbation).

(from 0 to 100 kHz) and tracing the fast ion orbits. The resonance between a rotating perturbation and the fast ions is thus taken into account in the above sense, which has been shown to slightly increase the fast ion loss rate as reported in figure 10. On the other hand, the drift kinetic effect of fast ions on the internal kink instability (which again depends on the mode-particle resonance) is not considered in this work. Physics studies of this effect have been extensively carried out in the literature. The above two-way resonant interactions can be studied within the linear stability analysis.

However, the nonlinear evolution of fishbone and the associated fast ion redistribution is not studied in the present work. Such nonlinear interactions, which often lead to the mode frequency chirping, have again been studied in literature e.g. in [55, 56] for ITER. Such a study is beyond the capability of the computational tools (MARS and ORBIT) employed in this work.

Figures 11(a) and (b) present, respectively, the redistribution of NBI fast ions in the particle phase space in the regions of $0 < s \leqslant 0.05$ and $0.05 < s \leqslant 0.12$. In Figure 11(a), the number of NBI fast ions with the energy around 1 MeV and pitch angle around 0.8 decreases the most in the region of $0 < s \leqslant 0.05$ in the presence of 100 kHz perturbation. Figure 11(b) shows that most of the increased NBI fast ions in the region of $0.05 < s \leqslant 0.12$ have an energy of about 800 keV and a pitch angle of about 0.8.

Combining the information in figure 11, it can be seen that in the presence of 100 kHz perturbation, most of the NBI fast ions transported from $0 < s \leqslant 0.05$ to $0.05 < s \leqslant 0.12$ have a decrease in energy from about 1 MeV to about 800 keV, while the pitch angle is not changed. This indicates that the energy of fast ions will be changed by the perturbation with frequency during the transport in this region, but the pitch angle is not affected. Therefore, the orbit type of NBI fast ions remains unchanged and the orbit radius increases, allowing the fast ions to be transported outward for some distance.

To verify the conclusions from the real-space and phase-space redistribution, an NBI fast ion with an energy of 960 keV and pitch angle of 0.8 is taken in the region of
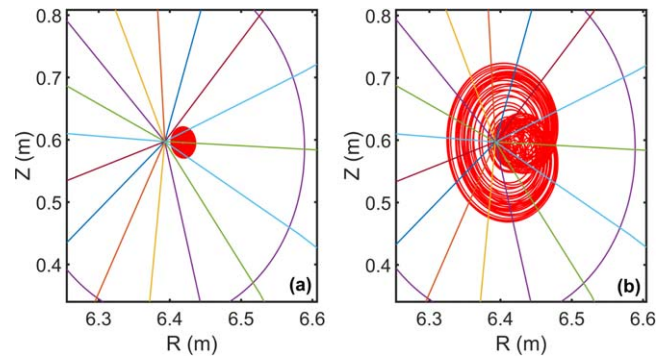
$0 < s \leqslant 0.05$. The orbit of a fast ion moving 5 ms in the presence of 0 and 100 kHz perturbations is calculated utilizing ORBIT. The calculation results are shown in figure 12. Figures 12(a) and (b) show, respectively, the NBI fast ion orbits on the R–Z plane in the presence of 0 and 100 kHz perturbations. Compared with 0 kHz perturbation, the orbit radius of the fast ion with 100 kHz perturbation is significantly larger and the orbit spans a larger region. This confirms that the NBI fast ions with the effect of 100 kHz perturbation do transport from $0 < s \leqslant 0.05$ to $0.05 < s \leqslant 0.12$ compared to the case of 0 kHz perturbation, resulting in a significant transport phenomenon in the plasma core region.

4.3. Effects of internal kinks with different toroidal mode numbers on NBI fast ion redistribution

In this section, the effect of internal kink modes with different toroidal mode numbers n on the redistribution of NBI fast ions is investigated. The perturbation amplitude $A = 500$ G and the perturbation frequency $f = 0$ are fixed, while the toroidal mode numbers are $n = 1, 2, 3, 4$.

Figure 13 presents the calculation results of ORBIT for different n. Figures 13(a)–(d) compare, respectively, the variation of the number profiles of NBI fast ions in real space with the $n = 1, 2, 3, 4$ internal kink mode perturbations and without perturbation. The four black vertical dotted lines in plots (a)–(d) represent the radial positions of $s = 0.32, 0.34, 0.36, 0.38$. The calculation results show that although the change of n does not affect the overall shape of NBI fast ion redistribution, the boundary of fast ions is related to n. When $n = 1, 2, 3, 4$, the NBI fast ions are transported, respectively, from the regions of $s \leqslant 0.32, 0.34, 0.36, 0.38$ to the regions of $s > 0.32, 0.34, 0.36, 0.38$.

The boundary of fast ion transport increases as n increases. Figures 13(e)–(h) show the relative change of NBI fast ion number in real space with different n. The relative change of NBI fast ion number is basically constant when n increases, while the region where fast ion transport occurs is gradually shifted outward in the radial direction. This shift of
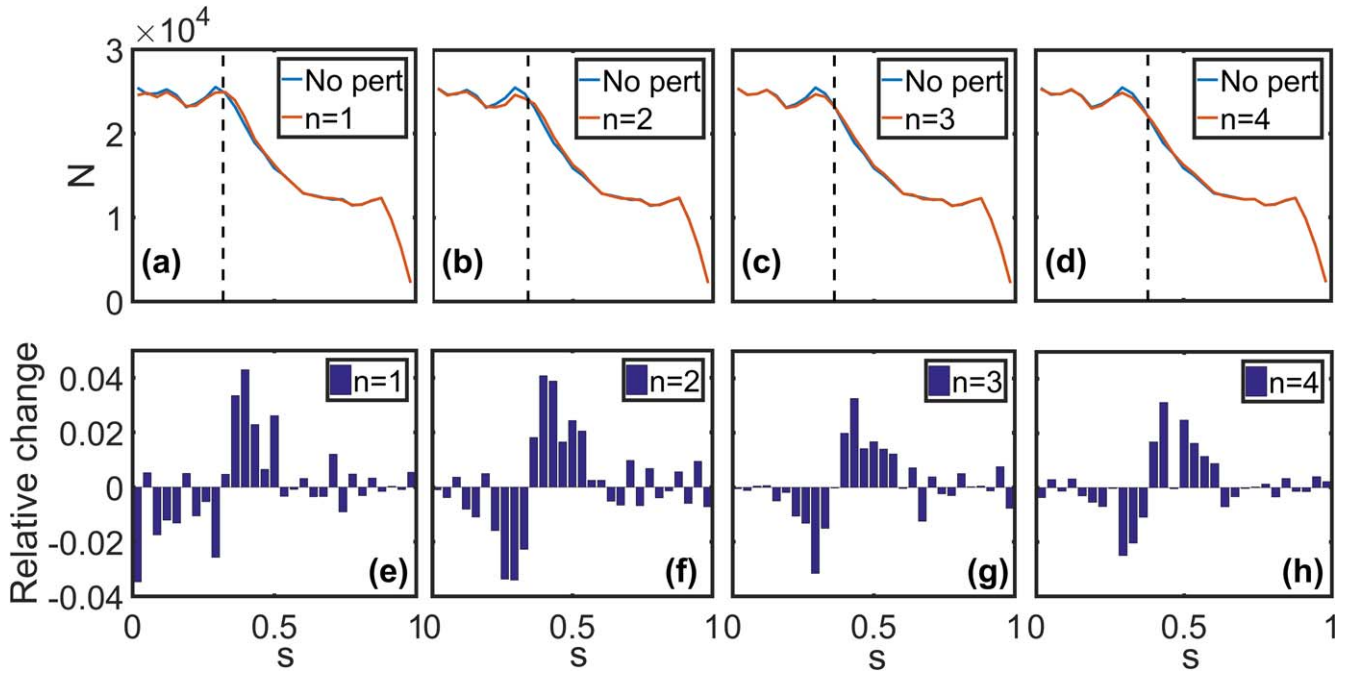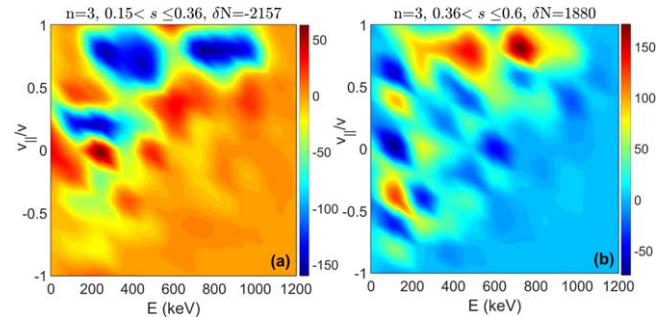
Figure 13. NBI fast ion number profiles in real space. The first row (a)–(d) shows the variation of NBI fast ion number profiles in real space in the presence of the perturbation amplitude $A = 500$ G, the perturbation frequency $f = 0$ internal kink perturbations with the toroidal mode number (a) $n = 1$, (b) $n = 2$, (c) $n = 3$, (d) $n = 4$. The second row (e)–(h) shows the relative change of NBI fast ion number in real space in the presence of the internal kink perturbations with the toroidal mode number (e) $n = 1$, (f) $n = 2$, (g) $n = 3$, (h) $n = 4$.
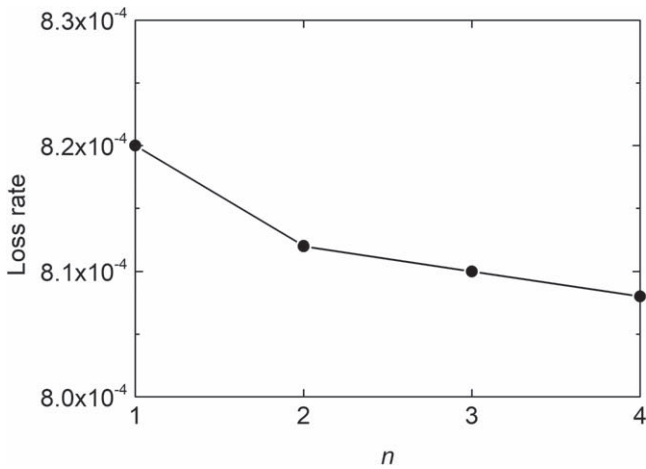
Figure 14. Relationship of NBI fast ion loss rate and the perturbation amplitude $A = 500$ G, the perturbation frequency $f = 0$ internal kinks with different toroidal mode numbers n. The fast ions are considered lost once they intersect the LCFS.

Figure 15. Distribution of NBI fast ion number change in the particle phase space ($E - v_{\parallel}/v$ plane) in the presence of the perturbation amplitude $A = 500$ G, the perturbation frequency $f = 0$, the toroidal mode number $n = 3$ internal kink perturbation. (a) Distribution in the real region of the radial position $0.15 < s \leqslant 0.36$. (b) Distribution in the real region of the radial position $0.36 < s \leqslant 0.60$.

transport region is related to the outward excursion of internal kink perturbations with different n along the radial direction, which is presented in figure 3.

The relationship curve between the loss rate of NBI fast ions and toroidal mode number n is shown in figure 14. It can be seen that the loss rate of fast ions is not affected by n. Similar conclusions are shown in sections 4.1 and 4.2 that the perturbation amplitude and frequency have no effect on the fast ion loss rate. As the internal kink/fishbone perturbation occurs mainly in the core region in ITER, which is a large-scale tokamak device, the transport of NBI fast ions with

perturbation is not sufficient to cause the fast ions to move to the plasma edge and escape from the plasma. Hence the internal MHD perturbation does not affect the loss of NBI fast ions in ITER.

Figure 15 presents the redistribution of NBI fast ions in the particle phase space in the regions of $0.15 < s \leqslant 0.36$ and $0.36 < s \leqslant 0.60$. Figure 15(a) shows that in the presence of the $n = 3$ internal kink mode perturbation, NBI fast ions in the region of $0.15 < s \leqslant 0.36$ with the largest number reduction have the pitch angle around 0.8, while the energy is distributed between 700 keV and 1 MeV, and between 200 and 500 keV. Figure 15(b) shows that the number of NBI fast ions with pitch angle around 0.8 and energy around
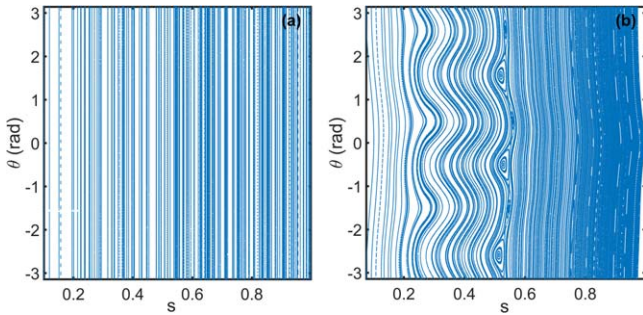
Figure 16. Real-space Poincaré diagram of NBI fast ion drift orbits with $E = 720$ keV and $v_\parallel/v = 0.8$. (a) Case without perturbation. (b) Case with the perturbation amplitude $A = 500$ G, the perturbation frequency $f = 0$, the toroidal mode number $n = 3$ internal kink perturbation.

700 and 500 keV increases the most. Thus the NBI fast ions are transported from $0.15 < s \leqslant 0.36$ to $0.36 < s \leqslant 0.60$ without any change in pitch angle, while the fast ion energy is changed by the perturbation.

The NBI fast ion with an energy of 720 keV and pitch angle of 0.8 is selected from the region where fast ion transport occurs in figure 15. The real-space Poincaré diagram is calculated and plotted. As figure 16(b) shows, the fast ion orbit is distorted in the region of $0.15 < s \leqslant 0.36$ where NBI fast ion transport occurs. The radial position is changed, and a magnetic island structure is present. This structure enables the NBI fast ions to cross from the left side to the right side of the magnetic island, which greatly enhances fast ion transport. Hence the transport of NBI fast ions from $0.15 < s \leqslant 0.36$ to $0.36 < s \leqslant 0.60$ is confirmed.

5. Conclusions

Redistribution of half a million of NBI fast ions by the ideal internal MHD instabilities in ITER has been simulated utilizing the tracing particle orbit code ORBIT. Three parameters associated with MHD perturbations are considered in this work: the perturbation amplitude A of the internal kink, the perturbation frequency f of the fishbone, and the toroidal mode number n of the internal kink. The effects of these parameters on the transport and loss of fast ions are investigated. The perturbation amplitude is assumed to be $A = 100, 300, 500$ G, the perturbation frequency is assumed to be $f = 0, 20, 40, 60, 80, 100$ kHz, and the toroidal mode numbers are $n = 1, 2, 3, 4$.

Redistribution of NBI fast ions is found to be sensitive to the perturbation amplitude and frequency. With the $n = 1$ internal kink perturbation, the NBI fast ions transport from the region of $0 < s \leqslant 0.32$ to $0.32 < s \leqslant 0.53$. The transport becomes greater as the perturbation amplitude increases. As the perturbation amplitude rises to 500 G, which is 1% of the background magnetic field in ITER, the maximum relative change of fast ion number in the radial position approaches 5%.

With respect to the effect of fishbone perturbation frequency, a strong fast ion transport occurs between the regions of $0 < s \leqslant 0.05$ and $0.05 < s \leqslant 0.12$, and higher frequency leads to stronger transport. When the perturbation frequency reaches 100 kHz, the number of fast ions in the region of $0 < s \leqslant 0.05$ is reduced by 30%.

The perturbation structure with different toroidal mode numbers n does not affect the relative change of the NBI fast ion number in real space. But as the value of n increases, the fast ion transport regions shift outward along the radial direction, which is consistent with the outward excursion of internal kink perturbations with different n in the radial direction.

As for the loss of NBI fast ions, we find that the loss number is independent of the perturbation amplitude A, the perturbation frequency f and the toroidal mode number n. This is because the internal kink mode/fishbone perturbation occurs in the core region in ITER, which is a device sufficiently large in size to allow particles to escape. Of course, fast ion loss may occur at (unrealistically) higher perturbation amplitude which we do not consider here. Transport induced by MHD perturbations considered in this work is not sufficient to cause the NBI fast ions to move to the plasma edge and escape from the plasma. Hence the ideal internal MHD perturbation does not affect the loss of NBI fast ions in ITER.

Although the NBI fast ion transport induced by 100 kHz fishbone perturbation can result in a maximum decrease of 30% in the relative value of fast ion number, the transport regions of $0 < s \leqslant 0.05$ and $0.05 < s \leqslant 0.12$ are still located in the core region of the plasma where the fusion reaction mainly occurs. Thus the strong transport of NBI fast ions triggered by high-frequency fishbone perturbations does not affect the NBI heating power and fusion condition in ITER. On the other hand, the particle transport from $0 < s \leqslant 0.32$ to $0.32 < s \leqslant 0.53$ can cause a 5% decrease in the fast ion number when the perturbation amplitude reaches 500 G. The influence of this kind of transport on the fusion condition of ITER needs further study in the future.

Appendix

Here are the specific expressions and equations applied by ORBIT. First, there are Hamiltonian quantities, Lagrangian quantities, Lagrangian equations, and magnetic field expressions for guiding center drift motion without perturbation:

$$H = \frac{\rho_\parallel^2 B^2}{2} + \mu B + \Phi \tag{A.1}$$

$$L = (\mathbf{A} + \rho_\parallel \mathbf{B}) \cdot \mathbf{v} + \mu \dot{\xi} - H \tag{A.2}$$

$$\frac{\mathrm{d}}{\mathrm{d}t}\frac{\partial L}{\partial \dot{q}} = \frac{\partial L}{\partial q} \tag{A.3}$$

$$\mathbf{B} = g\nabla\zeta + I\nabla\theta + \delta\nabla\psi_\mathrm{p}, \tag{A.4}$$

where $\rho_\parallel = v_\parallel / B$, represents the normalized parallel gyration radius of a particle; $\mu = v_\perp^2 / 2B$, represents the normalized magnetic moment of a particle; Φ is the electric potential. The magnetic field can be written as $\mathbf{B} = \nabla \times (\psi\nabla\theta - \psi_\mathrm{p}\nabla\zeta) = \nabla \times \mathbf{A}$, with $\mathbf{A} = \psi\nabla\theta - \psi_\mathrm{p}\nabla\zeta$ representing the magnetic vector potential; $\mathbf{v}$ denotes the guiding center velocity; ξ labels the cyclotron phase. q is the safety factor, $(\psi_\mathrm{p}, \theta, \zeta)$ is the magnetic surface coordinates used in ORBIT, ψ_p represents the poloidal flux coordinates, θ represents the poloidal angle, ζ represents the toroidal angle. From the above equations, the equations of particle motion without perturbation can be derived as:

$$\dot{\rho}_\parallel = -\frac{1 - \rho_\parallel g'}{D}\left((\mu + \rho_\parallel^2 B)\frac{\partial B}{\partial \theta} + \frac{\partial \Phi}{\partial \theta}\right) \tag{A.5}$$

$$\dot{\psi}_\mathrm{p} = -\frac{g}{D}\left((\mu + \rho_\parallel^2 B)\frac{\partial B}{\partial \theta} + \frac{\partial \Phi}{\partial \theta}\right) \tag{A.6}$$

$$\dot{\theta} = \frac{\rho_\parallel B^2}{D}(1 - \rho_\parallel g') + \frac{g}{D}\left((\mu + \rho_\parallel^2 B)\frac{\partial B}{\partial \psi_\mathrm{p}} + \frac{\partial \Phi}{\partial \psi_\mathrm{p}}\right) \tag{A.7}$$

$$\begin{aligned}
\dot{\zeta} = &\frac{\rho_\parallel B^2}{D}(q + \rho_\parallel(I'_{\psi_\mathrm{p}} - q\delta'_\theta)) \\
&- \frac{I}{D}\left((\mu + \rho_\parallel^2 B)\frac{\partial B}{\partial \psi_\mathrm{p}} + \frac{\partial \Phi}{\partial \psi_\mathrm{p}}\right) \\
&+ \frac{q\delta}{D}\left((\mu + \rho_\parallel^2 B)\frac{\partial B}{\partial \theta} + \frac{\partial \Phi}{\partial \theta}\right),
\end{aligned} \tag{A.8}$$

where

$$D = gq + I + \rho_\parallel(gI'_{\psi_\mathrm{p}} - Ig'_{\psi_\mathrm{p}} - gq\delta'_\theta + Iq\delta'_\zeta). $$

After considering the magnetic field perturbation, the perturbation in ORBIT takes the form:

$$\delta\mathbf{B} = \nabla \times \alpha\mathbf{B}, \tag{A.9}$$

where α is an arbitrary function of $\psi_\mathrm{p}, \theta, \zeta$, i.e. $\alpha = \alpha(\psi_\mathrm{p}, \theta, \zeta)$. From the modified canonical momentum, Hamiltonian, poloidal and toroidal canonical momentum:

$$\rho_\mathrm{c} = \rho_\parallel + \alpha \tag{A.10}$$

$$H = \frac{(\rho_\mathrm{c} - \alpha)^2 B^2}{2} + \mu B + \Phi \tag{A.11}$$

$$P_\theta = I\rho_\mathrm{c} + \psi \tag{A.12}$$

$$P_\zeta = g\rho_\mathrm{c} + \psi_\mathrm{p}. \tag{A.13}$$

The new motion equations can be obtained as:

$$\begin{aligned}
\dot{\rho}_\parallel = &\frac{\rho_\parallel^2 B + \mu}{D}\left(\left(-1 + \rho_\mathrm{c}g' + g\frac{\partial \alpha}{\partial \psi_\mathrm{p}}\right)\frac{\partial B}{\partial \theta}\right. \\
&\left. + \left(I\frac{\partial \alpha}{\partial \zeta} - g\frac{\partial \alpha}{\partial \theta}\right)\frac{\partial B}{\partial \psi_\mathrm{p}}\right) \\
&- \frac{q + \rho_\mathrm{c}I'}{D}\frac{\partial \Phi}{\partial \zeta} - \frac{1 - \rho_\mathrm{c}g'}{D}\frac{\partial \Phi}{\partial \theta} \\
&+ \frac{1}{D}\left(\frac{\partial \alpha}{\partial \psi_\mathrm{p}}\left(g\frac{\partial \Phi}{\partial \theta} - I\frac{\partial \Phi}{\partial \zeta}\right)\right. \\
&\left. + \frac{\partial \Phi}{\partial \psi_\mathrm{p}}\left(I\frac{\partial \alpha}{\partial \zeta} - g\frac{\partial \alpha}{\partial \theta}\right)\right) - \frac{\partial \alpha}{\partial t}
\end{aligned} \tag{A.14}$$

$$\begin{aligned}
\dot{\psi}_\mathrm{p} = &-\frac{g}{D}(\rho_\parallel^2 B + \mu)\frac{\partial B}{\partial \theta} + g\frac{\rho_\parallel B^2}{D}\frac{\partial \alpha}{\partial \theta} \\
&+ I\frac{\rho_\parallel B^2}{D}\frac{\partial \alpha}{\partial \zeta} - \frac{g}{D}\frac{\partial \Phi}{\partial \theta} + \frac{I}{D}\frac{\partial \Phi}{\partial \zeta}
\end{aligned} \tag{A.15}$$

$$\begin{aligned}
\dot{\theta} = &\frac{\partial H}{\partial P_\theta} \\
= &(\rho_\parallel^2 B + \mu)\frac{g}{D}\frac{\partial B}{\partial \psi_\mathrm{p}} + \frac{\rho_\parallel B^2(1 - \rho_\mathrm{c}g')}{D} \\
&- \rho_\parallel B^2\frac{g}{D}\frac{\partial \alpha}{\partial \psi_\mathrm{p}} + \frac{g}{D}\frac{\partial \Phi}{\partial \psi_\mathrm{p}}
\end{aligned} \tag{A.16}$$

$$\begin{aligned}
\dot{\zeta} = &\frac{\partial H}{\partial P_\zeta} \\
= &-(\rho_\parallel^2 B + \mu)\frac{I}{D}\frac{\partial B}{\partial \psi_\mathrm{p}} + \frac{\rho_\parallel B^2(q + \rho_\mathrm{c}I')}{D} \\
&+ \rho_\parallel B^2\frac{I}{D}\frac{\partial \alpha}{\partial \psi_\mathrm{p}} - \frac{I}{D}\frac{\partial \Phi}{\partial \psi_\mathrm{p}}
\end{aligned} \tag{A.17}$$

$$\dot{P}_\theta = -\frac{\partial H}{\partial \theta} = -(\rho_\parallel^2 B + \mu)\frac{\partial B}{\partial \theta} + \rho_\parallel B^2\frac{\partial \alpha}{\partial \theta} - \frac{\partial \Phi}{\partial \theta} \tag{A.18}$$

$$\dot{P}_\theta = -\frac{\partial H}{\partial \zeta} = \rho_\parallel B^2\frac{\partial \alpha}{\partial \zeta} - \frac{\partial \Phi}{\partial \zeta}. \tag{A.19}$$

The code ORBIT solves the above particle guiding center equations by the fourth-order Runge–Kutta method to obtain the orbits and distribution of particles.

ORCID iDs

Guanming YANG (杨冠铭) ⓘ https://orcid.org/0000-0002-5519-0134

References

[1] Heidbrink W W and Sadler G J 1994 *Nucl. Fusion* **34** 535
[2] Fasoli A *et al* 2007 *Nucl. Fusion* **47** S264
[3] Spong D A 2011 *Phys. Plasmas* **18** 056109
[4] Gorelenkov N N, Pinches S D and Toi K 2014 *Nucl. Fusion* **54** 125001
[5] White R B 1983 *Phys. Fluids* **26** 2958
[6] Von Thun C P *et al* 2010 *Nucl. Fusion* **50** 084009
[7] Kiptily V G *et al* 2017 *Nucl. Fusion* **58** 014003
[8] Muscatello C M *et al* 2012 *Nucl. Fusion* **52** 103022
[9] Van Zeeland M A *et al* 2013 *Plasma Phys. Control. Fusion* **56** 015009
[10] Garcia-Munoz M *et al* 2013 *Nucl. Fusion* **53** 123008
[11] White R B *et al* 2010 *Plasma Phys. Control. Fusion* **52** 045012
[12] Van Zeeland M A *et al* 2015 *Nucl. Fusion* **55** 073028
[13] Muscatello C M *et al* 2012 *Plasma Phys. Control. Fusion* **54** 025006
[14] Shen W *et al* 2014 *Phys. Plasmas* **21** 092514
[15] Kim D *et al* 2018 *Nucl. Fusion* **58** 082029
[16] Khan M *et al* 2012 *J. Fusion Energy* **31** 547
[17] Feng Z C, Qiu Z Y and Sheng Z M 2013 *Phys. Plasmas* **20** 122309
[18] Scott S D *et al* 2020 *J. Plasma Phys.* **86** 865860508
[19] Zhao R *et al* 2020 *Plasma Phys. Control. Fusion* **62** 115001
[20] Singh M J *et al* 2017 *New J. Phys.* **19** 055004
[21] Shimada M *et al* 2007 *Nucl. Fusion* **47** S1
[22] Von Thun C P *et al* 2012 *Nucl. Fusion* **52** 094010
[23] Tani K *et al* 2015 *Nucl. Fusion* **55** 053010
[24] Varje J *et al* 2016 *Nucl. Fusion* **56** 046014
[25] Sanchis L *et al* 2021 *Nucl. Fusion* **61** 046006
[26] Farengo R *et al* 2012 *Plasma Phys. Control. Fusion* **54** 025007
[27] Farengo R *et al* 2013 *Nucl. Fusion* **53** 043012
[28] Farengo R *et al* 2014 *Phys. Plasmas* **21** 082512
[29] Chen L, White R B and Rosenbluth M N 1984 *Phys. Rev. Lett.* **52** 1122
[30] White R B *et al* 1985 *Phys. Fluids* **28** 278
[31] Heidbrink W W *et al* 1986 *Phys. Rev. Lett.* **57** 835
[32] White R B *et al* 1988 *Phys. Rev. Lett.* **60** 2038
[33] Betti R and Freidberg J P 1993 *Phys. Rev. Lett.* **70** 3428
[34] Kolesnichenko Y I, Lutsenko V V and Marchenko V S 2000 *Nucl. Fusion* **40** 1731
[35] Wang S J 2001 *Phys. Rev. Lett.* **86** 5286
[36] Graves J P 2004 *Phys. Rev. Lett.* **92** 185003
[37] Fu G Y *et al* 2006 *Phys. Plasmas* **13** 052517
[38] He H D *et al* 2011 *Nucl. Fusion* **51** 113012
[39] Shen W *et al* 2015 *Phys. Plasmas* **22** 042510
[40] Wang X Q, Zhang R B and Meng G 2016 *Phys. Plasmas* **23** 074506
[41] Pei Y B *et al* 2017 *Phys. Plasmas* **24** 032507
[42] Yu L M *et al* 2019 *Nucl. Fusion* **59** 086016
[43] Von Thun C P *et al* 2011 *Nucl. Fusion* **51** 053003
[44] White R B and Chance M S 1984 *Phys. Fluids* **27** 2455
[45] Polevoi A, Shirai H and Takizuka T 1997 *Benchmarking of the NBI Block in Astra Code Versus the OFMC Calculations* (Tokyo: Japan Atomic Energy Research Institute JAERI-Data/Code 97-014)
[46] ITER Physics Expert Group on Energetic Particles, Heating and Current Drive and ITER Physics Basis Editors 1999 *Nucl. Fusion* **39** 2471
[47] White R B 2001 *The Theory of Toroidally Confined Plasmas* (London: Imperial College Press)
[48] Liu Y Q *et al* 2000 *Phys. Plasmas* **7** 3681
[49] Gude A *et al* 1999 *Nucl. Fusion* **39** 127
[50] Staebler A *et al* 2005 *Nucl. Fusion* **45** 617
[51] Chen W *et al* 2010 *Nucl. Fusion* **50** 084008
[52] Zheng T *et al* 2016 *Plasma Sci. Technol.* **18** 595
[53] Yu L M *et al* 2017 *J. Phys. Soc. Japan* **86** 024501
[54] Furth H P *et al* 1990 *Nucl. Fusion* **30** 1799
[55] Brochard G *et al* 2020 *Nucl. Fusion* **60** 086002
[56] Brochard G *et al* 2020 *Nucl. Fusion* **60** 126019